Experimental and numerical study on a new thermal masonry block by comparison with traditional walls

S. Summa [a],[*], G. Remia [b], C. Di Perna [b], F. Stazi [a]

[a] *Dipartimento di Scienze e Ingegneria della Materia, dell'Ambiente ed Urbanistica, Università Politecnica delle Marche, Ancona 60131, Italy*
[b] *Dipartimento di Ingegneria Industriale e Scienze Matematiche, Università Politecnica delle Marche, Ancona 60131, Italy*

ARTICLE INFO

ABSTRACT

The present work concerns an innovative construction system consisting of brick blocks with micropores and multiple air cavities which confer to the material a very low thermal conductivity combined with a high thermal inertia. The aim of this research is to experimentally compare the performance of these single-layer inertial walls with a traditional super-insulated lightweight wall, characterized by similar and very low steady thermal transmittance. The walls were monitored in the summer season in two adjacent test rooms in a free dynamic regime, i.e. without the use of mechanical cooling systems. The test rooms were built without windows to evaluate only the heat transfer through the opaque surface. The incidence of solar gains, of ventilation and of the dispersing surface area was evaluated by means of numerical analyses using the hourly dynamic method of EN ISO 52016-1. The results demonstrated that the new single-layer blocks with low conductivity and high thermal inertia guarantee excellent performance by substantially limiting the internal air temperature compared to the other solutions. This makes it possible to reduce the summer peak loads and cooling energy consumptions, especially in the case of night ventilation.

1. Introduction

European directives on energy saving have encouraged the construction of lightweight and super-insulated envelopes, which have proved to be unsuitable for the Mediterranean climate due to the onset of overheating problems and consequent increases in summer energy consumption. For this reason, recent regulations [1] have started to pay more attention to local climatic conditions as well as the indoor thermal environment, as demonstrated by the introduction of verification parameters such as surface mass and internal heat capacity, leading to a reconsideration of massive technologies. However, the parameters included in the same standards allow to consider alternatively either periodic thermal transmittance limits (Yie) or surface mass limits (Ms). In this way, it is possible to realize both massive walls, able to satisfy both verifications, and super-light walls which, through the adoption of very low values of steady thermal transmittance, reach the threshold values only for the first verification parameter. The advantages associated with the use of opaque envelope solutions with mass, in terms of environmental comfort and energy savings, are now recognized by the scientific community [2–5]. It has been demonstrated by parametric studies on numerous walls of equal transmittance, that the adoption of a

high inertia technology, with appropriate dynamic techniques to enhance its contribution (e.g. natural ventilation), can guarantee savings of up to 20% on cooling consumption and up to 10% on heating consumption [6]. The benefits of mass have also been demonstrated experimentally, using real case studies to calibrate parametric analysis software [5], or on-site test rooms through simultaneous measurements [7–10].

These studies, comparing technologies with different thermal inertia, concern archetypes of the sector, i.e. lightweight or mixed walls composed of independent layers of insulation and mass where the former can be external, in the cavity or on the internal envelope side.

As regards the insulation – mass position several studies demonstrated that structures with alternating layers of insulation and mass promote the accumulation of heat between the inner layers, improving the dynamic behaviour of the component [7,8].

However, the insulation layer could be expensive [9], could have problems of durability, open issues for inspection impossibility (in the case of cavity insulation), and problems related to the emission of toxic gases in the event of fire [10]. In order to overcome these constraints, several studies have focused on the incorporation of insulating materials within the vertical cavities or even better in the mixes of building blocks.

With regard to filling vertical holes in hollow bricks or hollow

* Corresponding author.
E-mail addresses: s.summa@univpm.it (S. Summa), g.remia@pm.univpm.it (G. Remia), c.diperna@univpm.it (C. Di Perna), f.stazi@univpm.it (F. Stazi).

Nomenclature		ggl,n	Global transmission factor of normal solar energy (-)
		ws	Wind speed (m\s)
T_a	Air temperature (°C)	*Subscript*	
T_s	Surface temperature (°C)	ext	external
$I_{g,h}$	Horizontal solar irradiance (W/m^2)	int	internal
Flux	Internal heat flux (W/m^2)	LW	light weight
λ	Thermal conductivity (W/(mK))	HW	heavyweight
c	Density (J/(kgK))	Max	maximum value
ρ	Heat capacity (kg/m^3)	Min	minimum value
M_s	Surface mass (kg/m^2)	w	window
f_a	Decrement factor (°C)	m	mean
φ	Time shift (hours)		
U	Thermal transmittance (W/m^{2}K)		

concrete blocks, materials such as EPS [11–13], perlite [14], compressed straw [15,16], hemp [17] or phase change microencapsulated material with diathonite [18] have been adopted.

With regard to blocks made with insulation mixes in the clay paste, a recent review [19] showed that this issue is attracting increasing interest since the use of insulating fillers obtained from waste materials would increase the envelope sustainability. For example research studies have been focused on concrete bricks with tyre rubber [20], clay bricks fired with 3 per cent palm kernel ash [21], terracotta bricks with the addition of waste marble dust [22], ceramic bricks fired with spent brewers' grains [23], clay bricks fired with expanded vermiculite[24], clay bricks fired with bagasse ash [25], bricks with paper residue [26], clay bricks fired with rice husk ash [27]. All these solutions present thermal conductivity values between 0.10 W/m K and 0.49 W/m K and density values between 615 kg/m^3 and 1660 kg/m^3.

Although, some of these solutions have been found to guarantee excellent performance with regard to winter energy efficiency, the thermal barrier effect achieved through the insulating additions could turn out to increase the summer conditioning consumptions. Recently [28] a research group participated to this open debate by exploring, through simulation of a residential building in 10 different climate zones in Chile, the thermo-physical properties of the materials able to guarantee annual operating temperatures within a specific comfort range (18 °C- 24 °C). The results of this study showed that the optimal material should have very low thermal conductivity values (approx. 0.03 W/(m•K)) and at the same time, very high density values (approx. 2500 kg/m^3). To date, however, building materials with these characteristics are still unknown because high densities typically correspond to high thermal conductivities and vice versa (e.g. concrete 2400 kg/m^3 and 1.63 W/(m•K), expanded polystyrene 25–70 kg/m^3 and 0.036 W/(m•K)).

To the authors' knowledge no studies were focused on the evaluation of the performance of building envelopes with this unusual simultaneous combination of high thermal capacity and low thermal conductivity in a single layer masonry. This type of solution could simplify the building design thus guaranteeing environmental sustainability for the simplification of the building construction phases and cloud allow significant energy saving.

This study focuses on a new 'diffuse insulation' envelope technology capable of guaranteeing simultaneously high thermal inertia and high thermal resistance, have been evaluated (Fig. 1). The envelope is realized through porous brick blocks fired with wood flour fillers, that during the combustion process, cause the formation of micro-cavities and provide the material with very low thermal conductivity. Furthermore, the presence of multiple air cavities alternating with numerous thin brick partitions determine not only excellent insulation, but also considerable thermal inertia.

The research aims to compare the performance of these new single-layer diffuse insulation inertial walls with traditional solutions also at the varying of solar gain and ventilation scenarios. To this aim the work involved a summer experimental campaign in two windowless test rooms in which the new wall has been compared with a super-insulated lightweight traditional wall characterized by similar and very low levels of steady thermal transmittance. Furthermore, numerical simulations allowed to evaluate the solutions under more realistic boundary conditions (increased solar gains for the presence of windows and natural ventilation) and to extend the comparisons to other multi-layered envelopes typical of the European building stock, for example the external thermal insulations composite systems (ETICS).

The paper is structured as follows: Section 2 describes the experimental and analytical methods used, while Section 3 analyses and discusses the results. Finally, Section 4 provides conclusions and proposals for future works.

Fig. 1. New 'diffuse insulation' envelope technology with high thermal inertia and low thermal conductivity.

2. Methods

2.1. General methodology

The flow chart in Fig. 2 summarises the activities carried out in this study.

2.2. Experimental method

The experimental work has been performed on two experimental rooms located in Ancona (lat:43.537; long:13.516), a city in central Italy (see Fig. 3). According to the Köppen-Geiger classification [29], this location is characterized by a humid subtropical climate (Cfa), while according to Presidential Decree 412/93 [30] Ancona falls in climate zone D with a number of Heating Degree Days (HDD) equal to 1688. The average monthly temperature of the coldest month is 5.7 °C, while that of the warmest month is 24.8 °C [31].

The two experimental rooms (see Fig. 4), identical externally, have a regular geometry characterized by width 3.00 m, length 3.30 m, height 3.13 m and gross volume of 31 m^3. There are no windows, interior partitions, or furniture, except for a table where the data acquisition station was set up. The rooms were built without windows in order to exclude the influence of the relative solar gains and consider only the phenomenon of heat transfer through the opaque envelope. The surrounding vegetation has been removed to avoid unwanted shading.

The perimeter walls, the roof and the foundations are identical both in geometry and in the type of materials used, except for the south-facing walls, which differ in mass and thermal inertia (see Fig. 5). The massive "HW" wall consists of new building blocks for infill masonry fired with wood flour fillers (layer 2), plastered internally and externally (layers 1 and 3) while the lightweight "LW" wall consists, starting from the outside, of a fiber cement layer (layer 1 in Fig. 5), an Oriented Strand Board (OSB) panel (layer 2), 24 cm thick rock wool (layer 3) and two plasterboard panels (layer 5), all supported by a framed metal structure.

The roofs and exterior walls facing north, east and west were built using sandwich panels consisting of two aluminium sheets and 12 cm thick rock wool, while the counter-ground slabs were made with a reinforced concrete foundation slab insulated with 8 cm of expanded polystyrene (EPS).

The thermophysical properties of the materials used for LW and HW walls, namely thermal conductivity (λ), density (ρ) and heat capacity (c), are given in Table1.

The brick block with wood fibers characteristics are reported in Table 2.

Table3 shows the thermo-physical characteristics of the structures constituting the building envelope of the experimental rooms. The thermal transmittance U was calculated according to EN ISO 6946:2018 [32], while the dynamic thermal characteristics (periodic thermal transmittance Y_{IE}, decrement factor f_a, phase shift ϕ, and internal heat capacity ki) were calculated according to EN ISO 13786:2018 standard

[33]. Finally, the surface mass Ms was calculated according to the following equation:

$$M_s = \sum_{i=1}^{n} \rho_i t_i \tag{1}$$

where:

ρ_i: density of the i-th layer of the opaque component considered (kg/m^3);
t_i: thickness of the i-th layer of the opaque component considered (m).

The monitoring was carried out from 12 July to 12 September 2022, and involved measuring the weather conditions and the climatic conditions inside the facilities (see Table 4). For each experimental room, six PT100-type platinum thermoresistances and a flowmeter were installed on the internal face of the south wall (see Fig. 6). The thermoresistances were used to monitor the indoor air temperature, the floor surface temperature, and the indoor and outdoor surface temperatures of the south wall at four different points (two outdoor and two indoor). Data acquisition was carried out using the DataTaker DT 500 Series 3 system with a 1-minute time step. The DataTaker DT 500 is an acquisition system with 10 analogue and 7 digital channels with 200 mA to 30 V open collector digital outputs and 3 high-speed counters. The system has an RS485 network with a maximum baud rate of 9600 Sy/s.

To monitor the outdoor weather conditions, a climate station was installed equipped with a series of sensors (see Table 4) capable of measuring outdoor air temperature, relative humidity, wind speed and direction, and normal, diffuse and global solar irradiance for all orientations near the experimental rooms. The global irradiance in the horizontal plane was evaluated in two ways: by a direct measurement using the spectrally flat pyranometer Class A according to ISO 9060:2018 (formerly "secondary standard") and by an indirect measurement coming from the acquisition of the normal solar irradiance and the diffuse irradiance obtained from the pyranometer and pyrheliometer contained in the RaZON + solar tracking system, both of Class C according to ISO 9060:2018. The calculated global horizontal irradiance was found to coincide with that directly measured one. The data acquisition interval of all the sensors is 1 min.

2.3. Numerical method (EN ISO 52016)

In this work, ICARO version 1.0.3.6 [34] was used to model the two test rooms previously described in Section 2.2. ICARO is a software for the hourly dynamic simulation of heating and cooling energy needs, indoor temperatures, and sensible and latent heat loads based on the calculation procedure contained in the EN ISO 52016–1:2017 standard [35]. The structure of this standard allows member countries to modify the calculation algorithm through National Annex A, which Italy used to improve the heat transfer method for opaque structures and the
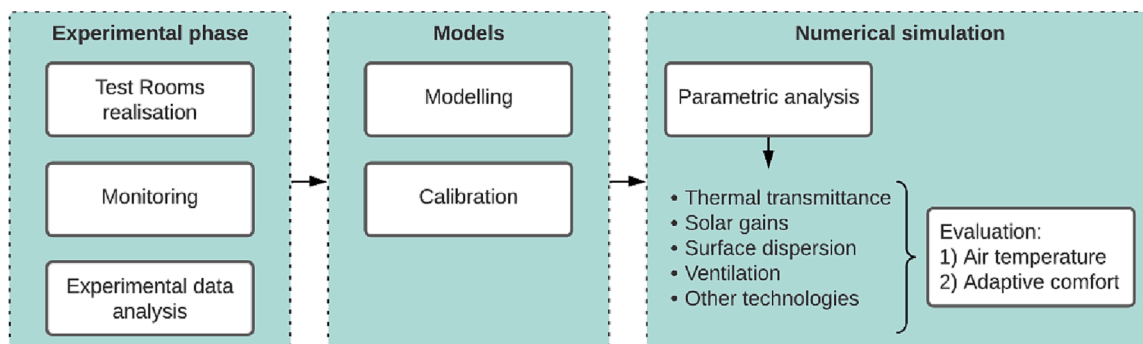

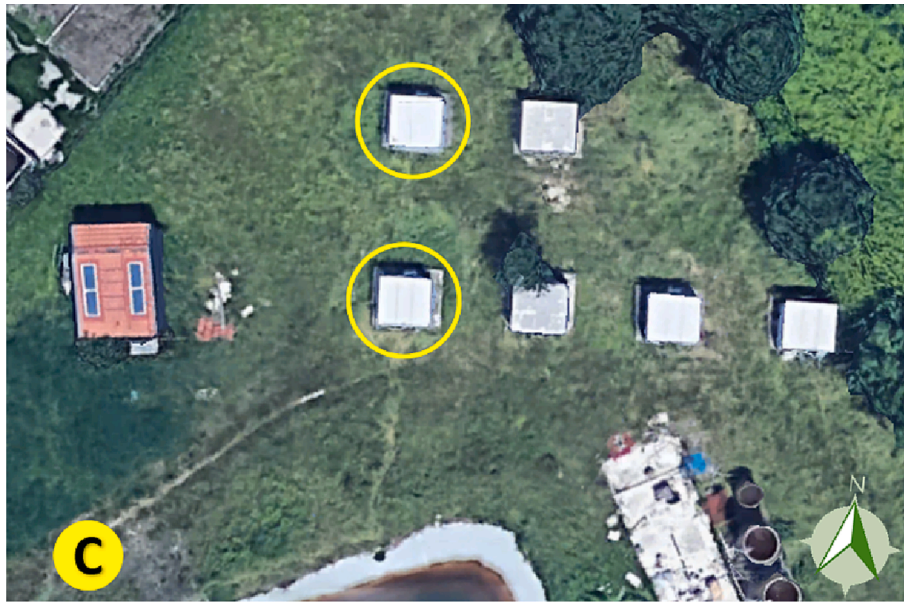**Fig. 2.** Flow chart of the experimental and numerical analyses.

Fig. 3. Site map. The test rooms used are circled and the letter 'C' indicates the position of the weather station.
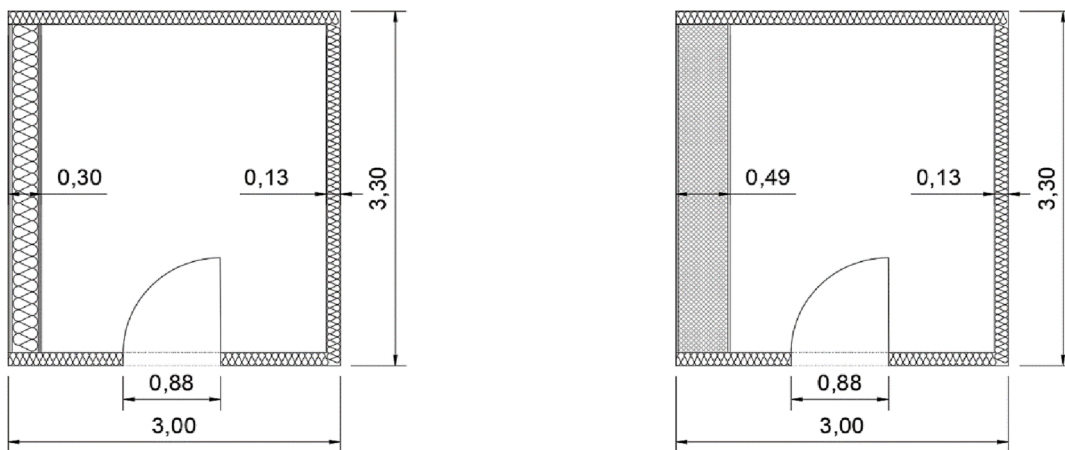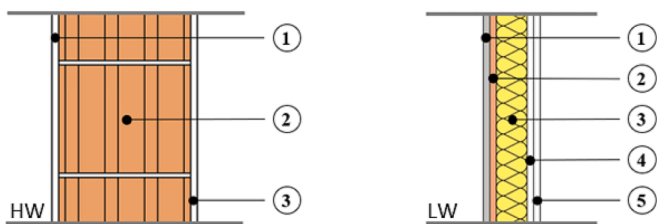

Fig. 4. Top view of the experimental rooms.

Fig. 5. Experimented walls, heavyweight new wall HW and lightweight wall LW.

Table 1
Thermophysical properties of materials.

Materials	t (cm)	λ (W/(mK))	c (J/(kgK))	ρ (kg/m³)
Plaster	2	0.900	1000	1800
Brick blocks	45	0.090	1000	830
Fibre-cement	1.6	0.420	1000	1600
OSB	2	0.130	1699	650
Rock wool	24	0.037	1029	100
Plasterboard panel	1.25	0.250	1000	900

Table 2
Dimensional, structural and acoustic characteristics of the new blocks studied.

Characteristics	Values
Size (mm)	450 × 250 × 199
Weight (Kg)	19,40
Compression strength fbk (N/mm²)	7.7
Soundproofing power Rw (dB)	52
Fire resistance (min)	240

calculation of solar contributions [36,37]. As regards the heat transfer model through opaque structures, the main differences between the standard and the Italian Annex consist in the number of capacitive nodes and resistive layers with which the lumped parameter RC network is modelled. The standard provides for a model consisting of a network of 5 capacitive nodes and 4 resistive layers, in which the areal heat capacity of the element is divided among the nodes according to the five foreseen positions of the thermal mass, while the conductance is attributed by 3/Rc to the two inner layers and by 6/Rc to the two outermost layers (with

Table 3
Thermal parameters of external walls and roof of experimental rooms.

Thermal Parameters	LW	HW	Other external wall	Roof
U (W/(m²K))	0.144	0.192	0.293	0.290
M_s (kg/m²)	85.10	445.50	25.50	25.50
Y_{IE} (W/(m²K))	0.072	0.001	0.276	0.273
f_a (-)	0.503	0.004	0.943	0.941
φ (h)	9.48	31.08	2.27	2.37
k_i (kJ/(m²K))	25.85	45.43	11.33	11.63

Rc = thermal resistance of the opaque element). Instead, the alternative methodology proposed in the Italian Annex, using the Fourier number (see Eq.1), provides for the modelling of an RC network that returns an appropriate number of capacitive nodes and resistive layers for each layer making up the opaque element.

$$Ncn_j = max\left[1; Int\left(\sqrt{\frac{Fo_{ref}}{Fo_j}} + 0.999999\right)\right] \qquad (2)$$

where:

$Fo_{ref} = \frac{\lambda_j}{\rho_j \bullet c_j} \bullet \frac{\Delta t}{d_j^2}$ number of capacitive nodes in the j-th layer.

λ_j thermal conductivity of layer material [W/(m K)].

ρ_j density [kg/m³].

c_j heat capacity per unit mass [J/(kg K)].

$\Delta t = 1h$ timestep [h].

d_j layer thickness [m].

$Fo_j = 0.5$ reference Fourier number.

The calculation according to the method provided by Italian Annex has been demonstrated to give better results than the one proposed in the European version of EN ISO 52016–1:2017 standard reducing the error on the internal flux amplitude between 14% and 67% [36]. For this reason, the simulations performed in this study have been carried out with the model of heat transfer through opaque elements contained in the Italian Annex.

2.3.1. Hourly dynamic simulations

Using the dynamic method of EN ISO 52016–1:2017 [35] with the heat transfer model of the opaque elements proposed in the Italian Annex, the models of the two test rooms were created, calibrated, and used to simulate the following scenarios (see Fig. 7):

Table 4
Sensors used in experimentation.

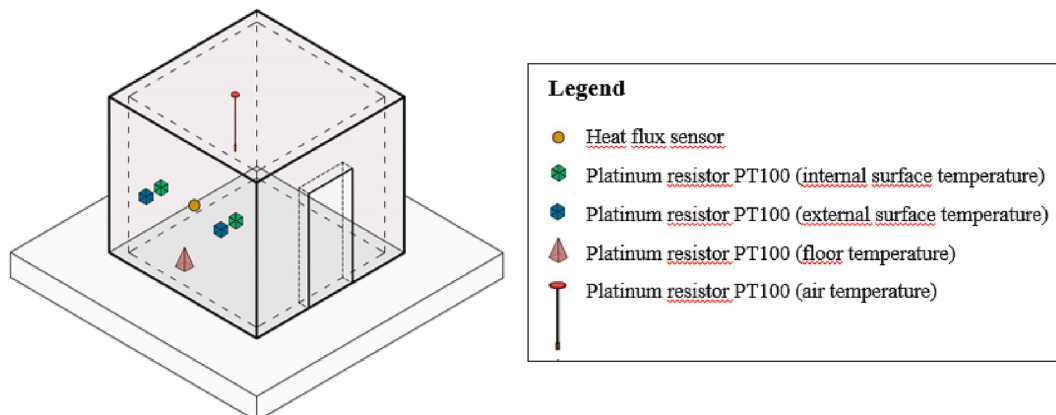| Measure	Sensor type	Model	Acquisition system	Rating	Position	Range	Accuracy
Indoor environmental conditions							
Air temperature	Platinum resistor	PT100	Datataker	1 min	Centre of the room H 1.80 m	− 40 °C ÷ + 80 °C	0.05 °C
Surface temperature	Platinum resistor	PT100	Datataker	1 min	South wall (internal side) H 1.40	− 40 °C ÷ + 80 °C	0.05 °C
Surface temperature	Platinum resistor	PT100	Datataker	1 min	South wall (internal side) H 1.40	− 40 °C ÷ + 80 °C	0.05 °C
Surface temperature	Platinum resistor	PT100	Datataker	1 min	South wall (external side) H 1.40	− 40 °C ÷ + 80 °C	0.05 °C
Surface temperature	Platinum resistor	PT100	Datataker	1 min	South wall (external side) H 1.40	− 40 °C ÷ + 80 °C	0.05 °C
Surface temperature	Platinum resistor	PT100	Datataker	1 min	Floor	− 40 °C ÷ + 80 °C	0.05 °C
Heat flux	Thermopile	HFP01	Datataker	1 min	South wall (internal side) H 1.40	± 2000 W/m²	± 3%
Outdoor environmental conditions							
Air temperature	Thermo hygrometer	HMT330	Elog	1 min	Climatic station	− 70 °C ÷ + 180 °C	± 0.2 °C
Relative humidity	Thermo hygrometer	HMT330	Elog	1 min	Climatic station	0 ÷ 100%	± 1%
Wind velocity	Anemometer	WMT700	Elog	1 min	Climatic station	0 ÷ 75 m/s	/
Wind directions	Anemometer	WMT700	Elog	1 min	Climatic station	0 ÷ 270°	/
Global solar irradiance_Horiz.	Pyranometer	SR30-M2-D1	RS-485	1 min	Climatic station	0 ÷ 4000 W/m²	< 2%

Legend

⬤ Heat flux sensor

✦ Platinum resistor PT100 (internal surface temperature)

✦ Platinum resistor PT100 (external surface temperature)

▲ Platinum resistor PT100 (floor temperature)

⬤ Platinum resistor PT100 (air temperature)

Fig. 6. Positions of the sensors installed in the experimental rooms.

1. Determine and compare the air temperature inside the test rooms adopting the massive HW envelope and a lightweight envelope of equal thermal transmittance called LW' on all four walls. The LW' envelope was obtained by starting from the LW wall described in Section 2.2 and decreasing the thermal insulation from 24 cm to 18 cm in order to have a thermal transmittance of 0.192 W/m²K, as for HW wall (see Fig. 7, Table 2 and Table 5);

2. Determine and compare the air temperature inside the test rooms using the envelopes defined in step 1 and adding a window on the south wall of 1.5 m² with frame factor 0.8, $U_w = 1.0$ W/m²K and $g_{gl} = 0.8$;

3. Determine and compare the air temperature inside the test rooms using the opaque and glazed envelope defined in step 2 and improving the solar transmission coefficient of the window to $g_{gl} = 0.35$;

4. Determine and compare the temperature of the air inside the test rooms using the opaque and glazed envelope defined in step 3 and making the east and north walls and slabs adiabatic as if to simulate a room with two external facing walls, on the southern and western sides.

5. Determine and compare the temperature of the air inside the test rooms using the envelopes defined in step 4 and increasing the natural ventilation (free cooling) flow rates to 2.5 ACH from 6 pm to 6 am.

Moreover, a detailed analysis was carried out to verify the incidence of dynamic parameters, namely the decrement factor and the internal areal capacity. To this aim, two other walls were designed and simulated (see Fig. 8, Tables 5 and 6): (i) IM wall that consists in an external thermal insulation composite (ETIC) system characterized by the same internal heat capacity and thermal transmittance of HW wall but with higher decrement factor, as in traditional applications; (ii) HW⁺ wall in which the internal plaster of HW wall was replaced with a clay finishing panel. The HW⁺ has the same decrement factor and thermal transmittance of the HW wall but higher internal areal heat capacity. These additional walls were evaluated only considering the scenarios 4 and 5.

2.4. Calibration method

The following metrics were used to calibrate the model created with the ICARO software [34]:

CVRMSE (Coefficient of Variation of the Root-Mean-Square Error) is used to assess how well an energy model is able to describe the measured data. According to ASHRAE guideline 14 [38], an hourly energy model is considered accurate if the CV(RMSE) value is less than 30%.

$$CVRMSE = \frac{\sqrt{\left(\sum_{i=1}^{n} \frac{(M_i - S_i)^2}{n}\right)}}{\overline{M}} \bullet 100 \, [\%] \qquad (3)$$

where Mi and Si are respectively the measured and simulated hourly surface temperatures, n is the number of hours in the considered interval and $\overline{M}$ is the average of the measured hourly data.

NMBE (Normalized Mean Bias Error) is used to scale the results of MBE, making them comparable. Generally, it is a good indicator of the overall behaviour of the simulated data with regards to the regression

Table 5
Thermophysical properties of materials of simulated external walls Table.

Materials	thickness (cm)	λ (W/(mK))	c (J/(kgK))	ρ (kg/m³)
Plaster	2	0.900	1000	1800
Fibre-cement	1.6	0.420	1000	1600
OSB	2	0.130	1699	650
Mineral wood	18	0.037	1029	100
Plasterboard panel	1.25	0.250	1000	900
Insulation XPS	12	0.034	1452	30
Hollow clay blocks	30	0.208	1000	295
Clay board	4	0.590	1100	1400

line of the sample. According to ASHRAE [38], this value can vary by up to 10%.

$$NMBE = \frac{1}{\overline{M}} \bullet \sum_{i=1}^{n} \frac{(M_i - S_i)}{n} \bullet 100 \, [\%] \qquad (4)$$

R^2 (coefficient of determination) is another statistical index commonly used to measure model uncertainty. Simulated values tending towards 1 indicate a perfect match with measured values. According to ASHRAE [38], this value must never be less than 0.75.

$$R^2 = \left(\frac{n \bullet \sum_{i=1}^{n} M_i \bullet S_i - \sum_{i=1}^{n} M_i \bullet \sum_{i=1}^{n} S_i}{\sqrt{\left(n \bullet \sum_{i=1}^{n} M_i^2 - \left(\sum_{i=1}^{n} M_i\right)^2\right) \bullet \left(n \bullet \sum_{i=1}^{n} S_i^2 - \left(\sum_{i=1}^{n} S_i\right)^2\right)}} \right)^2 \, [-] \qquad (5)$$

From the graph in Fig. 9, the measured air temperatures (x-axis) are related to the simulated temperatures (y-axis) within the two test rooms. In the case of the room with the LW wall, the simulated temperatures are overestimated on average by 3.4 °C, while in the case of the room with the HW wall, the simulated temperatures are underestimated on average by 1.9 °C. The smaller error in the HW room is also reflected in the coefficient of determination (R^2), which is slightly higher, even though in both cases this index is verified because it is above 75% (see Table 7).

Referring to Table 7, in addition to the coefficient of determination, the CVRMSE index is also largely verified for both models, especially from the HW wall room, while the NMBE index is verified for the HW room and slightly above the limit for the LW room. Despite the latter result, both models can be considered calibrated.

2.5. Adaptive thermal comfort model (EN 16798–1:2019)

The adaptive thermal comfort model developed for Europe [39] is included in EN 16798–1:2019 [40], which establishes three increasing categories of thermal comfort - categories I, II and III - each of which identifies different recommendations for use: category I is recommended for users with less thermal adaptation (e.g. elderly, sick or children), while categories II and III are recommended for new and existing buildings, respectively. Subsequent comfort categories incorporate the previous comfort categories (i.e., Cat.II incorporates Cat.I and Cat.III incorporates Cat.I and II), resulting in cumulative increasing percentages, while Discomfort hours are those obtained by subtracting the percentage of hours from Cat.III at 100%.
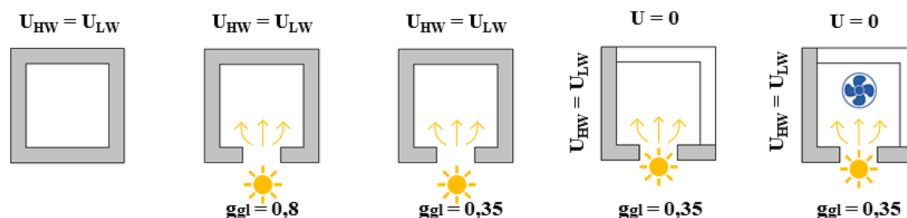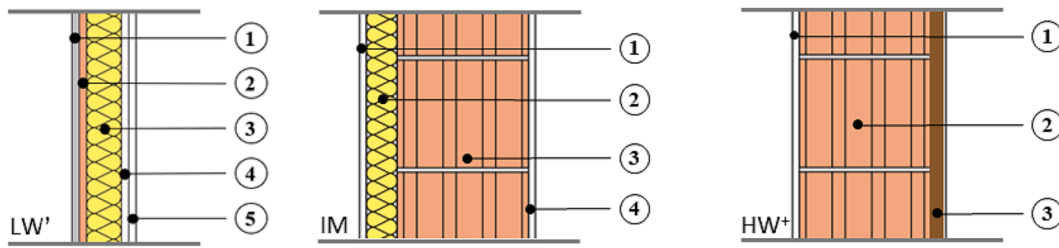

Fig. 7. Simulated scenarios.

Fig. 8. Simulated walls: LW': lightweight with the same thermal transmittance of wall HW; IM: traditional ETIC systems with internal mass; HW$^+$: heavyweight new wall with increased internal areal heat capacity.

Table 6
Thermal parameters of simulated external walls.

Thermal Parameters	HW	LW'	IM	HW$^+$
U [W/(m^{2}K)]	0.192	0.192	0.192	0.192
M$_s$ [kg/m^2]	445.50	78.7	165.4	447.50
Y$_{IE}$ [W/(m^{2}K)]	0.001	0.135	0.041	0.001
f$_a$ [-]	0.004	0.707	0.211	0.004
φ [h]	31.08	6.58	11.23	31.73
k$_i$ [kJ/(m^{2}K)]	45.43	25.59	45.44	53.45

In addition, each category sets lower and upper temperature limits for the indoor operating temperature, calculated using linear regression with respect to the 'running mean' outdoor air temperature (Trm). This represents a linear combination of the daily average temperatures of the previous days, calculated daily. The model is applicable when Trm is within the range between 10 ∘C and 30 ∘C.

The discomfort hours method requires calculating the percentage of hours when the indoor operating temperature falls outside a defined comfort range according to the specific category.

3. Results and discussion

3.1. Experimental analysis

The summer monitoring period from 12 July to 12 September showed very high external temperature values that exceeded the maximum expected for this area according to the Köppen and Geiger classification of 28.4 °C [41]. Indeed, during the 62 days of acquisitions, the outside air temperature (see Fig. 10) surpassed 30 °C in 45 days (i.e. 72.6%) and 35 °C in 8 days (i.e. 12.9%), reaching a maximum temperature of 38.2 °C on 23 July. Regarding solar irradiance on the horizontal plane, the maximum and average values achieved were 928 W/m2 and 391 W/m2 respectively. These temperatures and irradiances influenced the air temperature inside the two test rooms, which recorded average values and standard deviations for the entire monitoring period of 29.9 ± 3.3 °C and 28.5 ± 2.7 °C, for the LW and HW, respectively.

3.1.1. Air and surface temperatures

In the graphs of Figs. 11–13, a frequency analysis is carried out (cumulative and noncumulative), which makes it possible to identify with what frequency surface and internal air temperatures values are reached in the two test rooms.

In parallel with the analysis of what happens inside the structures, it is also essential to understand the ability of the structures to re-radiate thermal energy outwards and to influence the external microclimate, because this, in addition to favouring the Urban Heat Island phenomenon, negatively affects the cooling energy demand of buildings increasing their peak electricity demand and energy consumption [42]. The analysis of the external surface temperature of buildings appears to

Table 7
Statistical indexes for the validation of the simulated model.

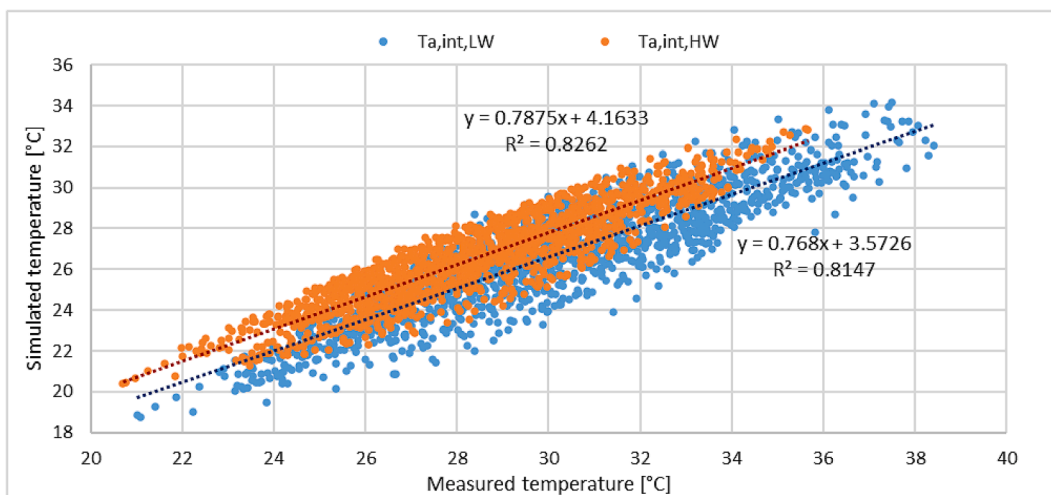| Statistical Index	Limit	Test room	Value
CVRMSE	≤30%	LW	12.2%
		HW	7.7%
NMBE	≤10%	LW	11.3%
		HW	6.6%
R^2	≥75%	LW	81.5%
		HW	82.6%

Fig. 9. Simulated and measured indoor air temperature trends of the test room with light (LW) and massive (HW) walls. The dotted lines represent the linear regressions of each data set.
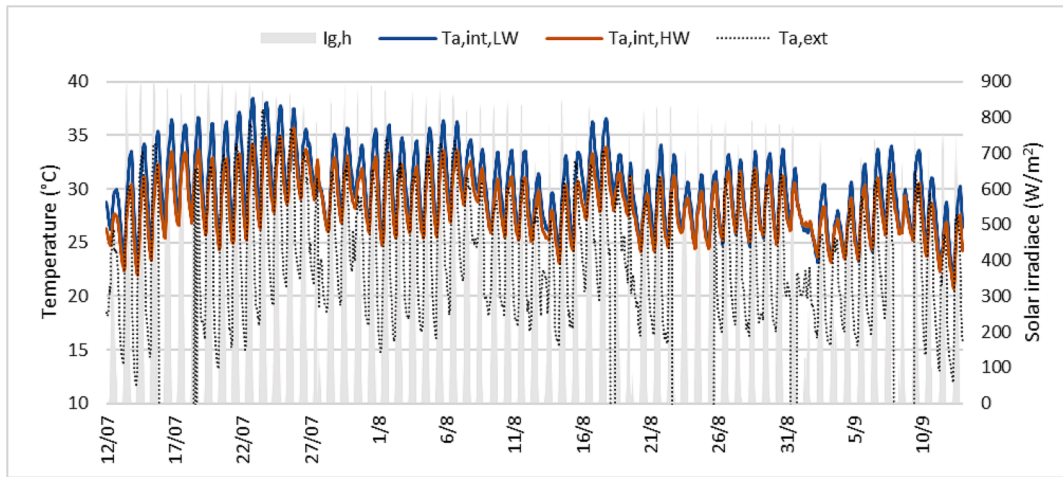
Fig. 10. Hourly trends of solar irradiance on the horizontal surface (Ig,h), outside air temperature (Ta,ext), air temperature inside the lightweight structure (Ta,int, LW), and air temperature inside the massive structure (Ta,int,HW). Period 12/07/2022–11/09/2022.
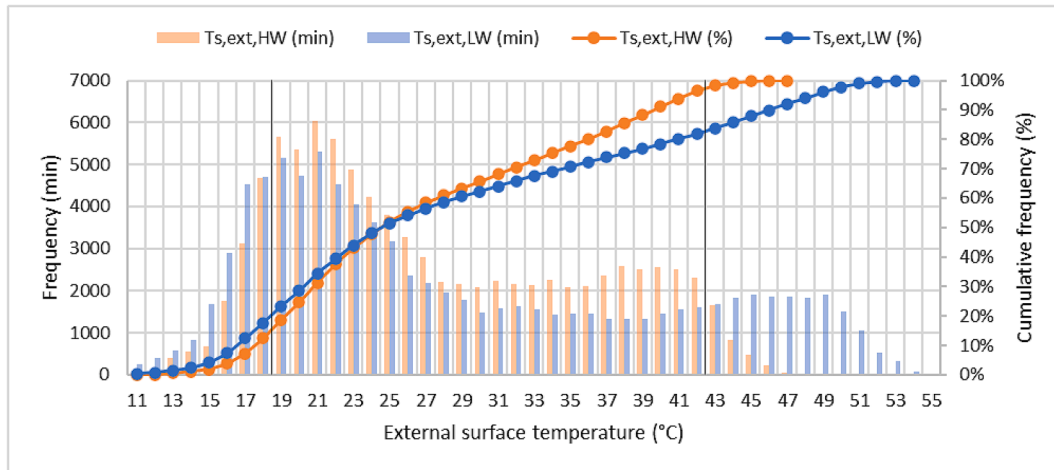

Fig. 11. Sample frequency (minutes) and cumulative frequency of external surface temperature of massive wall and lightweight wall. Period: July 20–25, 2022.
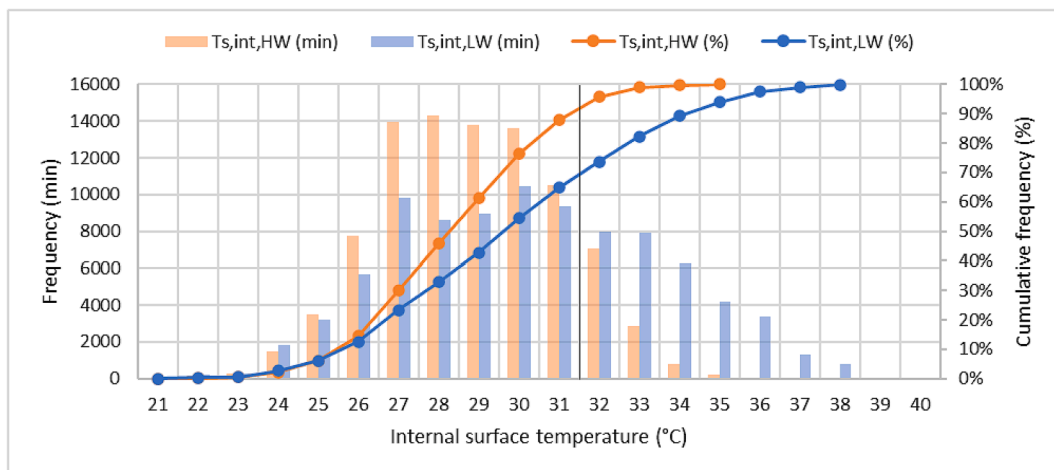

Fig. 12. Sample frequency (minutes) and cumulative frequency of internal surface temperature of massive wall and lightweight wall. Period: July 20–25, 2022.

be a central variable in climatological studies [43], which is why the external surface temperatures of the two test rooms were also monitored (see Fig. 11). The graph shows a maximum of 47.4 °C for the HW envelope and 54.3 °C for the LW one. The minimum external surface

temperatures, on the other hand, were more similar and were 11.8 °C and 10.3 °C for HW and LW respectively.

As regards the temperature frequency distribution, for the same number of measurements made, the graph in Fig. 11 mainly shows three
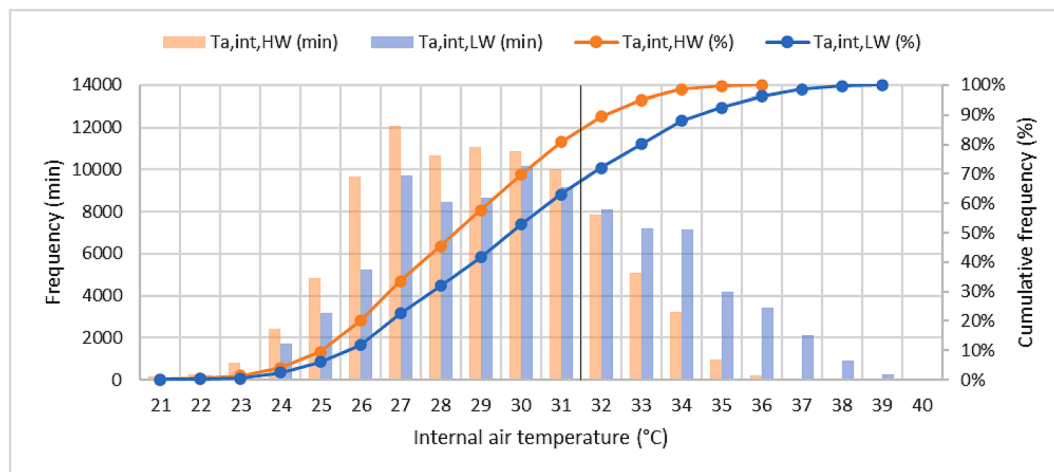
Fig. 13. Sample frequency (minutes) and cumulative frequency of internal air temperature of massive wall and lightweight wall. Period: July 20–25, 2022.

trends:(i) the first, from 11 °C to 18 °C, where the frequency of the external surface temperature of the LW wall is higher than that of the HW wall; this temperature range represents the night-time period in which, in the absence of solar radiation, there is a cooling, albeit slight, greater in the LW structure than in the HW one; (ii) the second, from 19 °C to 42 °C, where the frequency of the external surface temperature of the HW wall is higher than that of the LW wall; and (iii) the third, from 42 °C to 54 °C, where the frequency of the external surface temperature of the LW wall is much higher than that of the HW wall. The second and third temperature ranges represent the daytime period in which the presence of summer solar radiation leads to strong overheating of the external surfaces, especially for the LW wall. Overall, 52.5 % of the times Ts,ext,HW < Ts,ext,LW with an average delta of 3.7 °C, and 47.5 % of the times Ts,ext,LW < Ts,ext,HW with an average delta of 0.9 °C.

However, looking at the cumulative frequency curves (Fig. 11) and assuming an indoor air comfort temperature and indoor surface temperature of 26 °C, the incoming heat flux is null for 54.1% and 55.4% of the time for LW and HW, respectively. It can also be noted that the divergence of the two curves is very small (less than5%) up to an external surface temperature of 32°, and then increases up to a maximum delta of 14.6% at a surface temperature of 42 °C, where the non-exceedance percentage is 81.9% for the LW structure and 96.4% for the HW structure.

By looking instead at what happens inside the test rooms, we can analyse the internal surface temperature and the internal air temperature. Regarding the internal surface temperature (see Fig. 12), the HW and LW walls respectively record a maximum value of 34.4 °C and 38.0 °C and a minimum internal surface temperature of 21.7 °C and 21.0 °C. Regarding the temperature distribution, the graph in Fig. 12 shows two main trends: (i) the first, from 21 °C to 31 °C, where the frequency of the internal surface temperature of the HW wall is greater than that of the LW wall, and (ii) the second, from 32 °C to 40 °C, where the frequency of the internal surface temperature of the LW wall is much greater than that of the HW wall. Overall, 83.8 % of the times Ts,ext,HW < Ts,ext,LW with an average delta of 1.8 °C, and 16.2 % of the times Ts,ext,LW < Ts,ext,HW with an average delta of 0.4 °C. Observing the cumulative frequencies (Fig. 12), the two curves do not diverge by more than 5% up to the temperature of 26 °C, to then increase significantly up to a maximum delta of 23.1% corresponding to the internal surface temperature of 31 °C, where the percentage of not exceeding this temperature for the two walls is 64.8% for the LW envelope and 87.9% for the HW one.

The internal surface temperature graph is similar to the internal air temperature graph (see Fig. 13). The maximum air temperatures reached in the two test rooms differ by 2.7 °C and are respectively

35.7 °C and 38.4 °C for HW and LW, while the minimum air temperatures are almost comparable with 20.6 °C for HW and 20.9 °C for LW. Compared to the previously analysed surface temperatures, where the LW envelope reaches lower minimum temperatures than the HW envelope, in the case of air temperatures, the HW structure guarantees both lower minimums and lower maximums than the LW structure.

Also in this case the temperature distribution (see Fig. 13) shows two main trends: (i) the first, from 21 °C to 31 °C, where the frequency of the air temperature inside the HW room is higher than that of the LW room, and (ii) the second, from 32 °C to 39 °C, where the frequency of the surface temperature inside the LW room is greater than that of the HW wall. Unlike the internal surface temperature, the difference between the air temperatures of the two test rooms is less pronounced because it is influenced by the surface temperatures of the other walls (see Section 2.2). For this reason, the cumulative frequencies curves are also less differentiated from each other, reaching a maximum delta of 17.7% at a temperature of 31 °C, where the probability of not exceeding this value for the two test rooms is 63.0% for the LW envelope and 80.8% for the HW one. Instead, in the case of a comfort temperature of 26 °C, the probability of not exceeding this value is 11.8% for the LW room and 20.2% for the HW room.

A more detailed analysis of the results focused on the hottest period of the experimental campaign, i.e. from 20/07/2022 to 25/07/2022 (see Fig. 14), where 45.8 % of the time the outdoor temperatures were been above 30 °C until the maximum value of 38.2 °C was reached on 23/07/2022. Analysing the summer week in Fig. 14, the different behaviour between the two test rooms is evident: internal air temperature trend of LW is always higher than that of the HW, with a minimum delta between peaks of 1.8 °C and a maximum delta of 4.2 °C on 25/07 and 22/07 respectively.

Observing also Table 8, where the average values of the measured climatic parameters are shown, it can be seen that the deltas (Ta,LW - Ta, HW) between the two structures are greater in the presence of higher solar irradiance combined with low wind speed and air temperature, while the deltas between the two test rooms are lower in the presence of high external air temperatures, medium–low wind speeds and low solar irradiances. Therefore, it can be stated that the different internal thermal response of the two test rooms is mainly caused by solar radiation, the meteorological parameter that characterises the dynamism of the summer season. The HW wall, compared to the LW, responds better to this dynamism thanks to a higher internal heat capacity value (see Table3), a greater energy storage capacity in the inner layers of the wall, a more efficient thermoregulation of the indoor environment, a better mitigation capacity of the incoming heat wave, and therefore a less significant indoor air heating rate. As also indicated in other works of literature [44–46], it can be stated that thermal inertia can favour better thermal
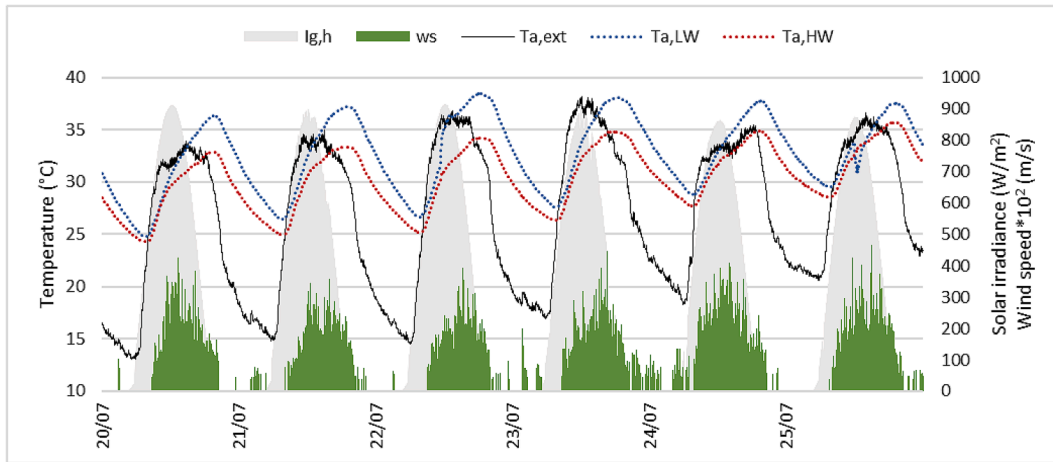
Fig. 14. Measured minute values of horizontal solar irradiance (W/m^2), wind speed (m/s), outdoor air temperature (°C), and indoor air temperature (°C) of the light and massive building during the heat wave July 20–25, 2022.

Table 8
Average values of outdoor temperature, horizontal solar irradiance, wind speed and air temperature in the two test rooms. Period July 20–25, 2022. Parameters that induce high temperatures in test rooms (i.e. high external air temperature, high solar irradiance and low wind speed) are highlighted in dark red, vice versa in dark blue.

Data	Ta,ext	Ig,h	ws	Ta,LW	Ta,HW	Ta,LW - Ta,HW
	°C	W/m^2	m/s	°C	°C	°C
20/7	24.5	328.3	0.61	30.7	28.8	1.9
21/7	25.5	317.2	0.55	32.1	29.5	2.6
22/7	26.4	324.5	0.52	33.0	30.0	3.1
23/7	28.0	309.2	0.62	33.2	30.9	2.3
24/7	27.9	303.0	0.78	33.3	31.4	2.0
25/7	28.5	304.2	0.66	33.4	32.1	1.3

comfort inside structures and corresponding energy savings.

Focusing on the day 23/07 when the maximum outdoor temperature was reached, two other dynamic thermal parameters can be observed: the attenuation in amplitude of the thermal wave (fa) and the phase shift of the thermal wave (φ), i.e. the period of time between the maximum value of the thermal stress and the maximum of its effect.

Analysing Figs. 15 and 16 respectively, the different behaviour of the two test rooms under the same external climatic conditions is evident: (i) the LW wall is able to attenuate the temperature by 16.5 °C, reaching a

maximum internal surface temperature of 37.8 °C and shifting the thermal wave by 4 h 54 m; (ii) the HW wall, on the other hand, is able to attenuate the temperature by 14.0 °C, reaching a maximum internal surface temperature of 33.4 °C and shifting the thermal wave by 6h00m (+24 h). For the latter wall, however, it should be noted that the time lag is greater than 24 h and that the maximum effect in terms of internal surface temperature on 23/07 is caused by the maximum thermal stress produced on the previous day (consistent with Table 6).

3.1.2. Thermal flows

Confirming the results already obtained, the thermal flows show the benefits of the thermal inertia of the HW wall compared to the LW wall. In fact, under the same external climatic conditions, although the incoming heat fluxes of the HW wall are 11.99 kW/m^2 higher than those of the LW wall, the difference between the outgoing heat fluxes is greater and equal to 14.45 kW/m^2 (see Fig. 17). Having higher outgoing thermal fluxes than incoming ones means having lower internal surface temperatures as seen in the previous section.

3.2. Numerical analysis

Observing the graph in Fig. 18, it can be seen that each box plot, representing the different walls for the different scenarios presented in section 2.3.1, maintains a certain symmetry with respect to its own
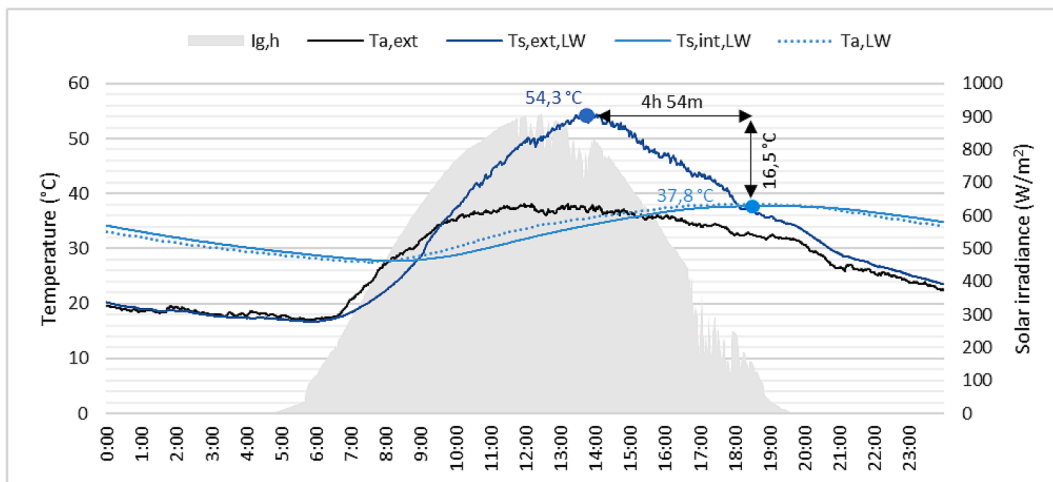

Fig. 15. Measured minute values of horizontal solar irradiance (W/m^2), outdoor air temperature (°C), and outdoor and indoor surface temperature (°C) of the lightweight building during the hottest day of the measurement campaign (July 23, 2022).

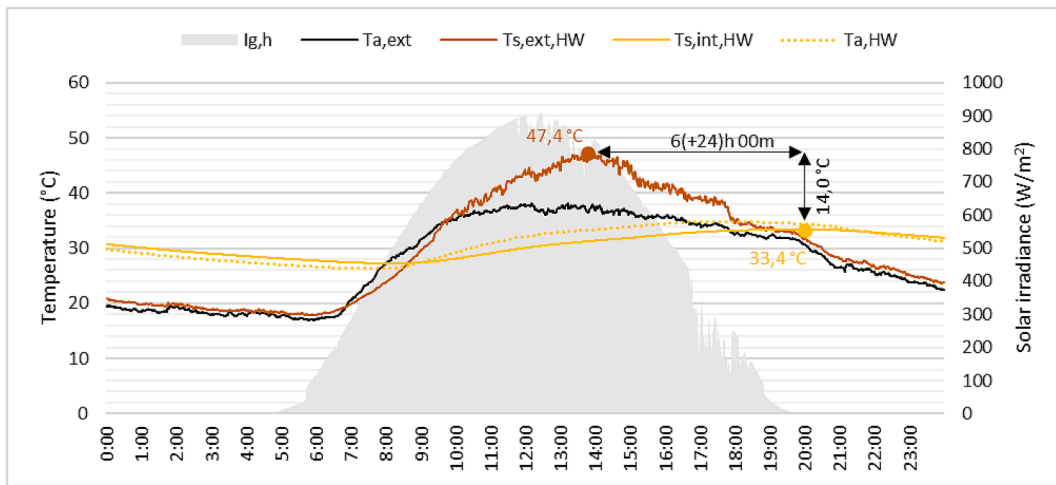**Fig. 16.** Measured minute values of horizontal solar irradiance (W/m²), outdoor air temperature (°C), and outdoor and indoor surface temperature (°C) of the massive building during the hottest day of the measurement campaign (July 23, 2022).
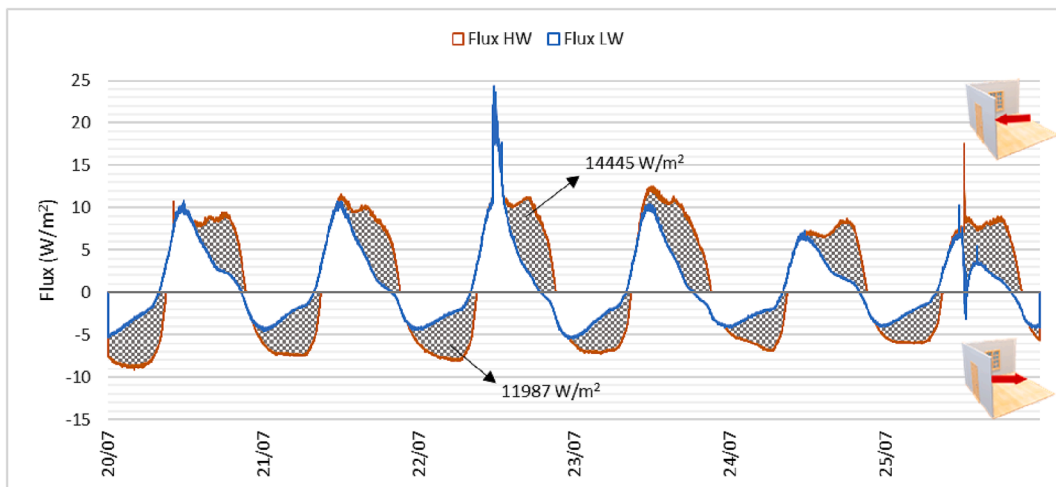

Fig. 17. Measured minute values of heat flux (W/m²) of the light and massive building during the heat wave July 20–25, 2022. The dotted area indicates the W/m² difference between the HW and LW wall heat fluxes.

median line and that the latter does not seem to deviate significantly from the arithmetic mean as there are no significant outliers.

As regards the results obtained from the numerical analyses, it can be observed that although for each scenario the averages and medians coincide between the different wall types proposed, the boxes heights, i. e. the interquartile difference, and the distance between the lower and upper whiskers, are always smaller for the walls with the greatest thermal inertia (HW and HW +). This indicates a smaller fluctuation and greater stability of the air temperatures inside the rooms as the external climatic conditions change.

With reference to Fig. 18, the individual scenarios are analysed below.

3.2.1. Extension of the studied envelopes to the entire perimeter of the test rooms

Compared to the experimental mock-up in which only one wall on the southern side was under study, extending HW and LW' to the entire test room (scenario 1) results in a decrease in maximum indoor air temperature of 6.7 °C and 6.4 °C, respectively. Obviously, the decrease of thermal transmittance over the entire room allows the conductive thermal exchanges to be limited, especially in the HW test room with high thermal inertia where the temperature excursion (difference

between the minimum and maximum value of the summer period under examination) is reduced by 67%, guaranteeing average internal air temperatures (Ta,m) of 26.8 °C ± 2.5 °C. In the case of the test room LW' on the other hand, 'scenario 1' limits the temperature excursion by 39%, guaranteeing a Ta,m of 26.7 °C ± 5.3 °C. This demonstrates that increasing the thermal resistance of the building envelope is generally indicated as the most crucial factor in reducing the building's energy demand, especially in climates dominated by heating [47], but in a transient situation, the thermal mass of a building may progressively absorb, store and release heat as a function of the temperature difference with the surrounding environment, showing a reduced reaction to an initial excitation (e.g. solar radiation)[48].

3.2.2. Presence of solar loads

By adding a medium-performance south window (scenario 2), the two test rooms again show significantly higher indoor air temperatures than in 'scenario 1'. The introduction of internal solar loads to hyper-insulated structures leads both HW and LW' structures to an increase in maximum indoor air temperatures of 10.9 °C and 11.7 °C, respectively, and an increase the seasonal temperature excursion of 8.5 °C and 17.5 °C, respectively. The Ta,m instead results to be 39.5 °C ± 4.3 °C for the HW room and 39.5 °C ± 8.8 °C for the LW' room.
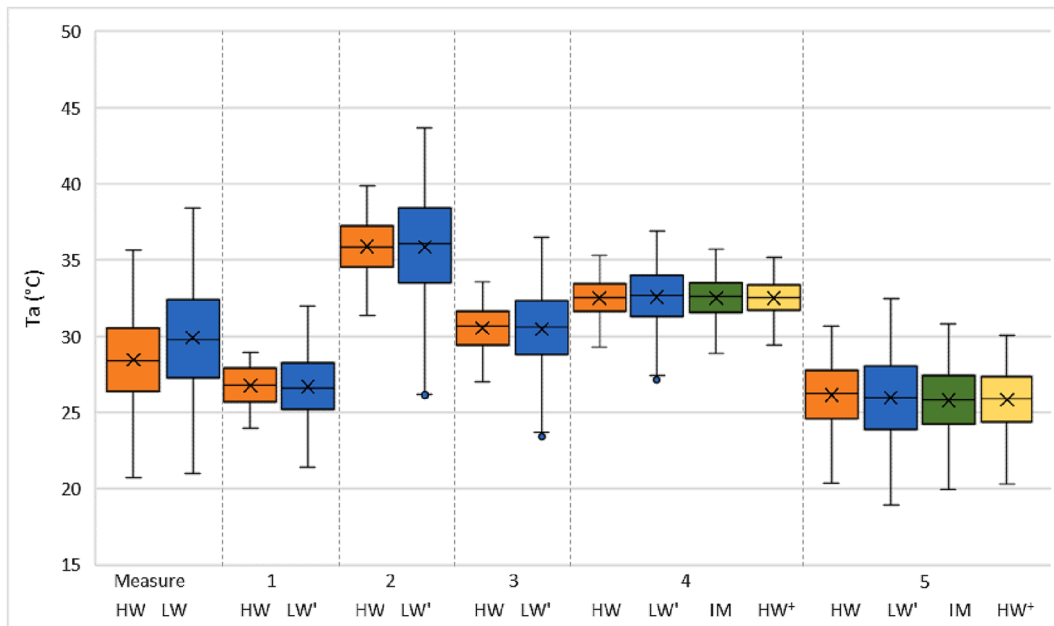
Fig. 18. Box plot of indoor air temperatures in test rooms for various proposed scenarios.

3.2.3. Optimisation of the glass surface

To overcome the problem of 'scenario 2′, it is decided to optimise the window by introducing selective glass in order to decrease the solar transmission coefficient g_{gl} from 0.8 to 0.35 (scenario 3). This solution, by decreasing the entry of heat by irradiation, makes it possible to guarantee lower average internal air temperatures compared to 'scenario 2′ and equal to 30.5 °C ± 3.3 °C for room HW and 30.5 °C ± 6.5 °C for room LW'. Again, the seasonal temperature excursion is greater for the low thermal inertia structure LW', showing a variation of 13.1 °C compared to 6.6 °C for the HW structure.

3.2.4. Simulation of a corner room in a flat and evaluation of alternative walls

To evaluate the solutions within a real space, the North and East walls and floors were made adiabatic, as if to simulate a corner room within an apartment on the middle floor of a multi-story building (scenario 4). In this scenario, since only the south and west walls are able to dissipate thermal energy by transmission, the average indoor air temperatures increase compared to the previous scenario by 2.0 °C and 2.1 °C respectively for the LW' and HW walls. A comparative analysis of the four walls used in this scenario shows once again that thermal inertia has a positive effect on the seasonal temperature range. In particular, the HW + wall, only by increasing its internal thermal capacity with respect to the HW wall (from 45.43 kJ/(m²K) to 53.45 kJ/(m²K)), allows the seasonal temperature excursion to be limited to 5.8 °C compared to 6.1 °C for the HW wall. IM and LW' follow with fluctuations in the internal air temperature of 6.9 °C and 9.8 °C respectively. Thermal inertia, in addition to reducing fluctuations in internal temperatures and thus the required peak energy, also allows the required air-conditioning load to be shifted, preventing the great problem of overloading electricity grids [49,50].

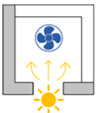### 3.2.5. Nocturnal free cooling

In order to decrease the average indoor air temperatures of 'scenario 4′, the adoption of direct night-time free cooling (scenario 5) was evaluated. By increasing the ACH, the Ta,m of all rooms decreased by about 20 % from 32.5 °C to 25.9 °C on average. Also for this scenario, the HW + room is the most advantageous in terms of overheating: the range of indoor air temperatures in which 50% of the values are positioned (interquartile difference) varies between 24.4 °C and 27.3 °C, while the

summer seasonal temperature excursion is 9.7 °C. Next, from best to worst, are the HW, IM and LW' rooms. This result, as already seen in other studies [51–53], makes it possible to confirm that appropriately pre-cooled thermal mass is capable of absorbing cold and releasing it when the temperature inside the structure increases, thus decreasing or shifting the peak demand of air-conditioning systems.

From the results obtained by evaluating the trends of the indoor air temperatures in the rooms of all scenarios, it was decided to analyse through the Adaptive Method of EN ISO 16798 [40] the comfort of the two configurations that provide the lowest overheating, i.e. scenario 1 and 5 (see Table 9).

In general, the data in Table 9 show that in the summer season, walls with a higher thermal inertia offer better indoor comfort performance. In particular in scenario 1, the absence of solar loads allows the HW room to have 100% of the hours in comfort in Cat.1, while the LW' room only 78% of the hours. For more realistic scenario 5, on the other hand, the HW + room, thanks to a minimal increase in internal thermal capacity and surface mass compared to the HW wall, is the best, guaranteeing 92% of the hours in Cat.1 against 88% for the HW room. Immediately after there is IM room and finally LW' room, which guarantees Cat.1 comfort for only 65% of the summer hours, i.e. 27% fewer

Table 9
Adaptive comfort assessment of scenarios 1 and 5.

Scenario	Wall	Comfort			Discomfort
		Cat.1	Cat.2	Cat.3	-
	HW	100%	100%	100%	0%
	LW'	78%	93%	98%	2%
	HW	88%	99%	100%	0%
	LW'	65%	88%	97%	3%
	IM	87%	98%	100%	0%
	HW⁺	92%	99%	100%	0%

hours than the HW + solid wall. Furthermore, in both scenarios, LW' room is the only one that also has discomfort hours.

These results are in line with those reported by other studies in the literature [28,54]. In particular, in the study [28], through a sensitivity analysis and the optimisation of the model of a standard building over 10 different climatic zones, it was obtained that the material that would allow the annual internal operating temperature to be maintained within the range of thermal comfort (18–24 °C) is a material that at the same time should have a thermal conductivity similar to that of expanded polystyrene (0.036 W/(m•K)), but density with values close to 2500 kg/m^3. As [28] states, materials with these characteristics are currently unknown, but the brick block with pores and wood fibres (HW) proposed in this study is capable of guaranteeing good values of both parameters (0.09 W/(m•K) and 830 kg/m^3). This new massive blocks with diffuse insulation show optimal performance in absence of solar gains, but in a more realistic scenario with high solar loads, the adoption on the inner side of a thin layer with augmented storing capacity thank to higher both density and conductivity values ($\lambda = 0.59$ W/(mK); $\rho = 1400$ kg/m^3) could provide significant benefits.

4. Conclusions

An experimental and numerical study was carried out on high performance innovative thermal masonry in comparison with traditional lightweight and massive solutions.

The summer monitoring showed that:

- The maximum air temperatures reached in the two test rooms are 35.7 °C and 38.4 °C for the HW and LW respectively, while the minimum air temperatures are almost comparable. As for the surface temperatures for 94.3 % of the times Ts,ext,HW < Ts,ext,LW with an average delta of 1.6 °C.
- The differences in air temperature values (Ta,LW - Ta,HW) between the two rooms are greater in the presence of higher solar irradiance combined with low wind speed and low outside air temperature. It can therefore be stated that the different internal thermal response of the two test chambers is mainly caused by solar radiation.

Having created and calibrated the model of the two test rooms, the numerical analysis showed that:

- The extension of both heavyweight and lightweight technologies to the entire test room (scenario 1) leads to a decrease in summer temperature excursion of 67% and 39%, respectively, compared to the experimental case study.
- The introduction of a south-facing glazed surface with medium performance (scenario 2) leads both heavyweight and lightweight envelopes to an increase in the mean indoor air temperatures up to 39.5 °C ± 4.3 °C and 39.5 °C ± 8.8 °C respectively. These temperatures are reduced by the adoption of selective glass (scenario 3).
- Simulating a corner room within an apartment on the middle floor of a multi-story building with a selective glazed window on the southern side (scenario 4) the best performance is achieved by the structures with the highest thermal mass and the highest internal heat capacity (HW$^+$).
- When night free cooling is added (scenario 5), the average indoor air temperature of all rooms is decreased by approximately 20%, from 32.5 °C to 25.9 °C. These temperatures also guarantee excellent comfort levels according to the adaptive model of EN ISO 16798.

In summary, from the results obtained both experimentally and numerically, the new single-layer block with low conductivity and high thermal inertia guarantees excellent performance limiting substantially the internal air temperature compared to other proposed solutions. However, in a realistic scenario with high solar loads, the addition of a thin clay layer (4 cm thick) with augmented storing capacity on the

inner wall side (wall HW$^+$) could provide even more benefits. Indeed, the high density ($\rho = 1400$ kg/m^3) and high conductivity ($\lambda = 0.59$ W/(mK)) of this clay panel increase the wall ability to interact with the indoor variations and to store internal heat. This makes it possible to limit summer thermal load peaks and cooling energy consumption, especially when integrated with night ventilation.

The future developments of this work will regard the monitoring of the new blocks during the winter period, and the evaluation of the summer period by installing the simulated clay panels and a glazed surface with programmed opening to verify the influence of solar gains and natural ventilation in the experimental phase. Furthermore, thanks to the installation of an air-conditioning system, it will be possible to test conditioning strategies for inertial structures in order to save energy during periods of maximum demand.

Declaration of Competing Interest

The authors declare that they have no known competing financial interests or personal relationships that could have appeared to influence the work reported in this paper.

Data availability

Data will be made available on request.

References

[1] Ministero dello sviluppo economico, "Italian iterministerial decree 26th June 2015: Application of calculation methods for energy performance and definition of minimum building requirements," *Off. Gazzette Ital. Repub. n°39 15th July 2015*, pp. 1–8, 2015.

[2] H. Sun, J.K. Calautit, C. Jimenez-Bescos, Examining the regulating impact of thermal mass on overheating, and the role of night ventilation, within different climates and future scenarios across China, Clean. Eng. Technol. 9 (2022), 100534, https://doi.org/10.1016/j.clet.2022.100534.

[3] E. Zilberberg, P. Trapper, I.A. Meir, S. Isaac, The impact of thermal mass and insulation of building structure on energy efficiency, Energy Build. 241 (2021), 110954, https://doi.org/10.1016/j.enbuild.2021.110954.

[4] E. Alayed, D. Bensaid, R. O'Hegarty, O. Kinnane, Thermal mass impact on energy consumption for buildings in hot climates: a novel finite element modelling study comparing building constructions for arid climates in Saudi Arabia, Energy Build. 271 (2022), 112324, https://doi.org/10.1016/j.enbuild.2022.112324.

[5] N. Aste, F. Leonforte, M. Manfren, M. Mazzon, Thermal inertia and energy efficiency – Parametric simulation assessment on a calibrated case study, Appl. Energy 145 (2015) (2015) 111–123, https://doi.org/10.1016/j.apenergy.2015.01.084.

[6] N. Aste, A. Angelotti, M. Buzzetti, The influence of the external walls thermal inertia on the energy performance of well insulated buildings, Energy Build. 41 (11) (2009) 1181–1187, https://doi.org/10.1016/j.enbuild.2009.06.005.

[7] M. Ibrahim, P. Achard, E. Wurtz, and P. H. Biwole, "Optimizing insulation-thermal mass wall layer distribution from maximum time lag and minimum decrement factor point of view," *Proc. BS 2013 13th Conf. Int. Build. Perform. Simul. Assoc.*, pp. 870–876, 2013, doi: 10.26868/25222708.2013.2009.

[8] K.J. Kontoleon, T.G. Theodosiou, K.G. Tsikaloudaki, The influence of concrete density and conductivity on walls' thermal inertia parameters under a variety of masonry and insulation placements, Appl. Energy 112 (2013) 325–337, https://doi.org/10.1016/j.apenergy.2013.06.029.

[9] B. Benazir, K. Kiran, M.S. Thanaraj, P. Selvaram, Partial replacement of cement in solid block by silico manganese dust, Int. J. Innov. Res. Technol. 6 (10) (2020) pp.

[10] V. Vitiello, R. Castelluccio, M. Del Rio Merino, Experimental research to evaluate the percentage change of thermal and mechanical properties of bricks in historical buildings due to moisture, Constr. Build. Mater. 244 (2020), 118107, https://doi.org/10.1016/j.conbuildmat.2020.118107.

[11] C. Hou, X. Meng, Y. Gao, W. Mao, E. Long, Effect of the insulation materials filling on the thermal performance of sintered hollow bricks under the air-conditioning intermittent operation, Case Stud. Constr. Mater. 8 (2018) 217–225, https://doi.org/10.1016/j.cscm.2018.02.007.

[12] Z. Pavlík, M. Jerman, A. Trník, V. Kočí, R. Černý, Effective thermal conductivity of hollow bricks with cavities filled by air and expanded polystyrene, J. Build. Phys. 37 (4) (2013) 436–448, https://doi.org/10.1177/1744259113499214.

[13] J. Li, X. Meng, Y. Gao, W. Mao, T. Luo, L. Zhang, Effect of the insulation materials filling on the thermal performance of sintered hollow bricks, Case Stud. Therm. Eng. 11 (2018) 62–70, https://doi.org/10.1016/j.csite.2017.12.007.

[14] M. Zukowski, G. Haese, Experimental and numerical investigation of a hollow brick filled with perlite insulation, Energy Build. 42 (9) (2010) 1402–1408, https://doi.org/10.1016/j.enbuild.2010.03.009.

[15] R. Ahmadi, B. Souri, M. Ebrahimi, Evaluation of wheat straw to insulate fired clay hollow bricks as a construction material, J. Clean. Prod. 254 (2020), 120043, https://doi.org/10.1016/j.jclepro.2020.120043.

[16] S. Hou, F. Liu, S. Wang, H. Bian, Coupled heat and moisture transfer in hollow concrete block wall filled with compressed straw bricks, Energy Build. 135 (2017) 74–84, https://doi.org/10.1016/j.enbuild.2016.11.026.

[17] M. Dlimi, R. Agounoun, I. Kadiri, R. Saadani, M. Rahmoune, Thermal performance assessment of double hollow brick walls filled with hemp concrete insulation material through computational fluid dynamics analysis and dynamic thermal simulations, e-Prime – Adv. Electr. Eng. Electron. 3 (2023), 100124, https://doi.org/10.1016/j.prime.2023.100124.

[18] Y. Fraine, C. Seladji, A. Aït-Mokhtar, Effect of microencapsulation phase change material and diatomite composite filling on hygrothermal performance of sintered hollow bricks, Build. Environ. 154 (2019) 145–154, https://doi.org/10.1016/j.buildenv.2019.02.036.

[19] D.S. Vijayan, A. Mohan, J. Revathy, D. Parthiban, R. Varatharajan, Evaluation of the impact of thermal performance on various building bricks and blocks: a review, Environ. Technol. Innov. 23 (2021), 101577, https://doi.org/10.1016/j.eti.2021.101577.

[20] E. Fraile-Garcia, J. Ferreiro-Cabello, M. Mendivil-Giro, A.S. Vicente-Navarro, Thermal behaviour of hollow blocks and bricks made of concrete doped with waste tyre rubber, Constr. Build. Mater. 176 (2018) 193–200, https://doi.org/10.1016/j.conbuildmat.2018.05.015.

[21] S. Hakkoum, A. Kriker, A. Mekhermeche, Thermal characteristics of Model houses Manufactured by date palm fiber reinforced earth bricks in desert regions of Ouargla Algeria, Energy Procedia 119 (2017) 662–669, https://doi.org/10.1016/j.egypro.2017.07.093.

[22] M. Sutcu, H. Alptekin, E. Erdogmus, Y. Er, O. Gencel, Characteristics of fired clay bricks with waste marble powder addition as building materials, Constr. Build. Mater. 82 (2015) 1–8, https://doi.org/10.1016/j.conbuildmat.2015.02.055.

[23] H. Bal, Y. Jannot, S. Gaye, F. Demeurie, Measurement and modelisation of the thermal conductivity of a wet composite porous medium: Laterite based bricks with millet waste additive, Constr. Build. Mater. 41 (2013) 586–593, https://doi.org/10.1016/j.conbuildmat.2012.12.032.

[24] M. Sutcu, Influence of expanded vermiculite on physical properties and thermal conductivity of clay bricks, Ceram. Int. 41 (2 Part B) (2015) 2819–2827, https://doi.org/10.1016/j.ceramint.2014.10.102.

[25] V. Mangesh, Madurwar, Sachin A. Mandavgane, Rahul V. Ralegaonkar, Development and feasibility analysis of bagasse ash bricks, J. Energy Eng. 141 (3) (2015).

[26] B. Mandili, M. Taqi, A. El Bouari, M. Errouaiti, Experimental study of a new ecological building material for a thermal insulation based on waste paper and lime, Constr. Build. Mater. 228 (2019), 117097, https://doi.org/10.1016/j.conbuildmat.2019.117097.

[27] G.H.M.J.S. De Silva, B.V.A. Perera, Effect of waste rice husk ash (RHA) on structural, thermal and acoustic properties of fired clay bricks, J. Build. Eng. 18 (2018) 252–259, https://doi.org/10.1016/j.jobe.2018.03.019.

[28] C. Avendaño-Vera, A. Martinez-Soto, V. Marincioni, Determination of optimal thermal inertia of building materials for housing in different Chilean climate zones, Renew. Sustain. Energy Rev. 131 (2020), 110031, https://doi.org/10.1016/j.rser.2020.110031.

[29] W. Köppen, R. Geiger, Das Geographische System der Klimate, Handb. der Klimatologie, 1936.

[30] President of the Republic, *Presidential Decree No. 412 of August 26, 1993*. Italy, 1993.

[31] Italian Organisation for Stardardisation (UNI), *UNI 10349-1:2016, Heating and cooling of buildings - Climatic data - Part 1: Monthly means for evaluation of energy need for space heating and cooling and methods for splitting global solar irradiance into the direct and diffuse parts and for calculate th*. Italy, 2016, p. 10349.

[32] International Organization for Standardization, "ISO 6946:2008 Building components and building elements - Thermal resistance and thermal transmittance - Calculation method," 2008.

[33] International Organization for Standardization, *ISO 13786:2008 Thermal performance of building components - Dynamic thermal characteristics - Calculation methods*. 2008.

[34] TEP srl, "ICARO." ANIT, 2021.

[35] International Organization for Standardization, *ISO 52016-1:2017 - Energy performance of buildings - Energy needs for heating and cooling, internal temperatures and sensible and latent heat loads – Part 1: Calculation procedures*. 2017, p. 204.

[36] L. Mazzarella, R. Scoccia, P. Colombo, M. Motta, Improvement to EN ISO 52016–1: 2017 hourly heat transfer through a wall assessment: the Italian National Annex, Energy Build. 210 (2020), 109758, https://doi.org/10.1016/j.enbuild.2020.109758.

[37] S. Summa, G. Remia, C. Di Perna, Comparative and sensitivity analysis of numerical methods for the discretization of opaque structures and parameters of glass components for EN ISO 52016–1, Energies 15 (3) (2022) pp, https://doi.org/10.3390/en15031030.

[38] ASHRAE Guideline 14, *Measurement of Energy, Demand, and Water Savings*. 2014, pp. 16–17.

[39] D. Bienvenido-Huertas, C. Rubio-Bellido, F. Farinha, M.J. Oliveira, J.L. Pérez-Ordóñez, Evaluating the potential of adaptive comfort approach using historic data to reduce energy consumption in buildings in southern Spain, Build. Environ. 185 (2020), https://doi.org/10.1016/j.buildenv.2020.107313.

[40] CEN European Commitee for Standardization, *EN 16798-1:2019 Energy performance of buildings - Ventilation for buildings - Part 1: Indoor environmental input parameters for design and assessment of energy performance of buildings addressing indoor air quality, thermal environment, lighting and acous*. 2019.

[41] "ClimateData.org.".

[42] X. Li, Y. Zhou, S. Yu, G. Jia, H. Li, W. Li, Urban heat island impacts on building energy consumption: a review of approaches and findings, Energy 174 (2019) 407–419, https://doi.org/10.1016/j.energy.2019.02.183.

[43] N. Benas, N. Chrysoulakis, C. Cartalis, Trends of urban surface temperature and heat island characteristics in the Mediterranean, Theor. Appl. Climatol. 130 (3) (2017) 807–816, https://doi.org/10.1007/s00704-016-1905-8.

[44] R. Hurt, R. Boehm, Y. Baghzouz, and a Cubano, "University of Nevada Zero Energy House Project," *ACEEE Summer Study Energy Effic. Build.*, pp. 128–138, 2006.

[45] L. Zhu, R. Hurt, D. Correia, R. Boehm, Detailed energy saving performance analyses on thermal mass walls demonstrated in a zero energy house, Energy Build. 41 (3) (2009) 303–310, https://doi.org/10.1016/j.enbuild.2008.10.003.

[46] K. Gregory, B. Moghtaderi, H. Sugo, A. Page, Effect of thermal mass on the thermal performance of various Australian residential constructions systems, Energy Build. 40 (4) (2008) 459–465, https://doi.org/10.1016/j.enbuild.2007.04.001.

[47] O. Kaynakli, A review of the economical and optimum thermal insulation thickness for building applications, Renew. Sustain. Energy Rev. 16 (1) (2012) 415–425, https://doi.org/10.1016/j.rser.2011.08.006.

[48] S. Verbeke, A. Audenaert, Thermal inertia in buildings: a review of impacts across climate and building use, Renew. Sustain. Energy Rev. 82 (2018) 2300–2318, https://doi.org/10.1016/j.rser.2017.08.083.

[49] L. Shen, Z. Li, Y. Sun, Performance evaluation of conventional demand response at building-group-level under different electricity pricings, Energy Build. 128 (2016) 143–154, https://doi.org/10.1016/j.enbuild.2016.06.082.

[50] J. Ma, J. Qin, T. Salsbury, P. Xu, Demand reduction in building energy systems based on economic model predictive control, Chem. Eng. Sci. 67 (1) (2012) 92–100, https://doi.org/10.1016/j.ces.2011.07.052.

[51] K. Lee, J.E. Braun, Model-based demand-limiting control of building thermal mass, Build. Environ. 43 (10) (2008) 1633–1646, https://doi.org/10.1016/j.buildenv.2007.10.009.

[52] W. Li, L. Yang, Y. Ji, P. Xu, Estimating demand response potential under coupled thermal inertia of building and air-conditioning system, Energy Build. 182 (2019) 19–29, https://doi.org/10.1016/j.enbuild.2018.10.022.

[53] L. Chahwane, L. Stephan, E. Wurtz, WITHDRAWN: assessment of an algorithm involving building thermal mass, indoor and outdoor mean running temperatures to enhance the control of night ventilation, Energy Build. (2018).

[54] C. Di Perna, F. Stazi, A.U. Casalena, M. D'Orazio, Influence of the internal inertia of the building envelope on summertime comfort in buildings with high internal heat loads, Energy Build. 43 (1) (2011) 200–206, https://doi.org/10.1016/j.enbuild.2010.09.007.